J. Fluid Mech. (2021), *vol*. 908, A42. © The Author(s), 2020.
Published by Cambridge University Press
doi:10.1017/jfm.2020.899

Investigation of shock dynamics in an axisymmetric inlet/isolator with attached boundary layers

Michael D. Leonard[1] **and V. Narayanaswamy**[1],†

[1]Department of Mechanical and Aerospace Engineering, North Carolina State University, Raleigh, NC 27695, USA

(Received 31 March 2020; revised 5 August 2020; accepted 11 October 2020)

Shock oscillations within a model two-dimensional axisymmetric inlet with a constant area isolator are investigated under the condition of maintaining an unseparated boundary layer throughout the inlet/isolator section. Power spectral densities of the wall-pressure fluctuations beneath each shock leg intersecting the isolator surface exhibited a very low frequency broadband oscillation in the 10–100 Hz range as well as a very high frequency broadband oscillations above 10 kHz. Whereas the high frequency oscillations are attributed to the incoming boundary layer fluctuations, detailed investigations into the pressure fluctuation communication pathways within the isolator and their length scale of communication are made to elucidate the origin of the low frequency fluctuations. It was found that the downstream propagation of pressure fluctuations is primarily by the convection of the boundary layer structures and this communication occurred over several boundary layer thicknesses. The upstream propagation occurs through acoustic waves that extend over a distance of one local boundary layer thickness. Based on this understanding, a physical model is constructed, which makes an accurate prediction of pressure power spectrum of the low frequency shock wave oscillations; the model predictions also favourably compare with the shock oscillations in external shock boundary layer interactions without shock-induced flow separation.

Key words: high-speed flow, compressible boundary layers, shock waves

1. Introduction

Shock boundary layer interactions have a pervasive occurrence in internal geometries such as scramjet inlets, isolators and nozzles of airbreathing vehicles and rockets at overexpanded conditions (Curran & Stull 1964). Typically, in scramjet inlets and isolators, flow compression occurs through a system of shock waves (called the 'shock train') most of which are contained within the duct resulting in multiple shock wave boundary layer interaction (SBLI) units. In contrast, the shock train in overexpanded nozzles typically contains very few SBLI units.

Because of the more common occurrence of shock trains within the duct in inlets and isolators, the rest of the discussion will pivot on the studies that were made in

† Email address for correspondence: vnaraya3@ncsu.edu

these flow units. From a design perspective, one needs to minimise the occurrence of flow separation anywhere in the duct while achieving the desired pressure increase with the geometric length constraints. This is one of the driving objectives of the scramjet inlet/isolator design where the boundary layer separation generated by the multiple shock intersections with the duct wall can generate large scale separated flow within the isolator and can mitigate the starting limits of the inlet. This shock system is known as a shock train and serves to decelerate the incoming supersonic flow and increase the pressure for efficient combustion. Many early studies explored the temporal mean features of the shock train, the individual shock structures and streamwise pressure variation for given inflow properties (Crocco 1958; Waltrup & Billig 1973; Ikui, Matsuo & Nagai 1974*a*; Carroll & Dutton 1990; Geerts & Yu 2016). Summarily, these studies showed that for a given back pressure, the shock trains were longer and comprised of multiple oblique shocks ('X' type) at high Mach numbers and confinement ratios. By contrast, the shock train was shorter and comprised of multiple normal shock waves at low Mach numbers and low confinement ratios. Previous investigations (Waltrup & Billig 1973; Carroll & Dutton 1990; Hunt & Gamba 2018) also showed that the maximum compression occurs at the most upstream shock leg and the subsequent shock legs make progressively smaller contribution to the overall flow compression. As a result, the separation onset occurs most commonly in the first shock leg; however, the smaller incoming Mach number of the subsequent shock legs elevates the propensity for separation in the subsequent legs as well.

In addition to the drag penalty, limitations to starting ability, etc., the shock induced separation also generates significant unsteady shock oscillations that result in accelerated fatigue of aerostructures, creation of hotspots within inlet/isolators operating at hypersonic speeds and high intensity aeroacoustic noise that is of a major public concern. The shock oscillations within the inlets can also feed into the combustion instabilities causing further reduction in safety margin. Hence, several previous efforts studied the shock oscillations that occur in inlet/isolators containing a separated flow within the duct. These studies can be broadly classified as those that investigate the naturally occurring shock oscillations when subject to a steady back pressure, and the ones that investigated the response of shock trains to forced periodic back pressure oscillations.

Ikui *et al.* (1974*a*,*b*) was among the first to report the natural shock oscillation power spectrum of the individual shock legs within the shock train. They showed the shock oscillation spectrum of the individual shock legs exhibit two prominent peaks, one at approximately 40 Hz, and the other in the 100–200 Hz range and negligible energy at higher frequencies. The spectra showed only a modest variation with duct inflow Mach number. The authors attributed the very low frequencies to the Helmholtz resonator type behaviour emanated from the settling chamber located downstream of the supersonic duct and the higher ($\sim$100 Hz) frequencies to the pressure waves set up within the duct by the characteristics. The authors also suggested a negligible role from the incoming boundary layer fluctuations. Yamane *et al.* (1984) measured the power spectrum of shock train oscillations within a duct subject to different back pressures that generated choked and unchoked conditions. Similar to Ikui *et al.* (1974*a*,*b*), Yamane *et al.* (1984) also reported the oscillation frequencies of the individual shock legs had a component below 100 Hz and another in the 100–300 Hz range; however, the oscillations below 100 Hz were observed only in the first shock leg. The authors discounted the Helmholtz resonator type behaviour from settling chamber as driving the shock train oscillation and instead proposed a new oscillation model that suggests a low-pass filter type behaviour in shock oscillations that stems from wall shear stress decelerating the shock motion. Sugiyama *et al.* (1988) made a direct visualisation of the shock train locations and oscillations

along with the boundary layer thickness in a semi-quantitative manner using schlieren imaging. They showed that, statistically, the oscillations in the boundary layer thickness correlated very well with the leading shock motions. They conjectured that the boundary layer variations emanate the oscillations in the leading shock, which is then propagated to the subsequent legs of the shock train. A similar suggestion was also made by Xiong *et al.* (2018) who showed that in a rectangular duct, the upstream shock oscillations feed the downstream shock leg oscillations. Interestingly, the authors also suggest that the separated flow downstream of the downstream shock leg does not contribute to the shock oscillations. More recent studies by Hunt & Gamba (2019) unravelled the complexity of the shock train oscillations and communications of pressure fluctuations within a rectangular duct subject to steady back pressure. Using a combination of multiple flow diagnostics, the authors successfully attributed different frequency bands and peaks to various sources and mechanisms that include upstream acoustic propagation of the back pressure fluctuations through the subsonic separated flow, interactions between separated flow units and boundary layers that develop over top/bottom walls, sidewall and wall junctions, contributions from the incoming boundary layer, separated flow pulsations that directly drive the local shock motions and downstream pressure fluctuation propagation between subsequent shock legs.

Previous studies that sought to capture how the combustion process impacts the shock train oscillations studied the effect of having unsteady back pressures on the shock train oscillations. To simplify the flow interactions, almost all the studies implemented a periodic back pressure oscillations of different amplitudes and the mean flow was typically separated in the isolator. Perhaps, the simplest yet highly insightful configuration was studied by Bruce & Babinsky (2008) wherein the authors subjected a single normal shock at transonic Mach number ($M = 1.4$ and 1.5) to back pressure oscillations. They showed that the response velocity of the shock oscillation in a constant area duct was to satisfy the instantaneous back pressure boundary condition. With this background, they further obtained an excellent agreement in the shock oscillation amplitude trend with frequency in both constant area and diverging ducts. Similar experiments with a shock train containing multiple shock waves showed several interesting similarities and differences. Su, Ji & Chen (2016) performed Reynolds-averaged Navier–Stokes (RANS) simulations in a Mach 6 inlet subject to different back pressure frequencies. They showed that, whereas shock oscillations effectively followed the back pressure trace on one wall, the presence of separation units on the other wall introduced other frequencies to the corresponding shock oscillations. They also showed that, whereas the shock oscillation response had the highest amplitude at low frequencies, the amplitudes quickly plateaued at higher frequencies, contrasting a decreasing trend obtained in the single shock studies (Bruce & Babinsky 2008). Su *et al.* (2016) also noted that the self-excited oscillation amplitudes are significantly smaller than the forced excitation amplitudes. Fiévet *et al.* (2017) performed direct numerical simulations (DNS) on a rectangular channel flow subject to periodic back pressure oscillations. Similar to Bruce & Babinsky (2008), Fievet *et al.* demonstrated that the shock structure underwent substantial changes during the upstream motion phase and downstream motion phase of the oscillations. They also found the existence of the resonant forcing frequency that elicited maximum shock oscillations and reported a 15 % increase in the shock oscillation amplitude at forcing frequency in the vicinity of the resonant frequency. They further showed that near the predicted resonant frequency, the shock legs at downstream end of the shock train respond the most to the back pressure oscillations compared to the shock waves around the leading edge of the shock train.

It is worthwhile to note that all the previous studies have focused on strongly back pressured inlets where the flow is separated over large or small areas within the duct. While this situation is fairly common in low to mid supersonic inlets, it may not be the

case in high supersonic and hypersonic inlets. This is because of the high inflow Mach number and a relatively benign pressure rise (relative to the inflow momentum) from the combustion process which causes the shock trains to occur without concomitant boundary layer separation. It is important to learn the unsteady features of these shock trains with unseparated boundary layers and the spectral nature of the boundary layer processed by the individual shock wave to obtain a reliable input on the location and strength of hot spots within the scramjet inlet/isolator, potential coupling with duct resonance, as well as the turbulent processes that occur within the duct, as all of these could impact the inlet design decisions. So far, there are no studies that have investigated the shock behaviour in unseparated internal flows while very few are available for external SBLI units (Smits & Muck 1987). The present work fills this knowledge gap using a canonical two-dimensional (2-D) constant area circular cross-section inlet/isolator that is devoid of the complicated junction flows of the planar inlets. Multiple flow diagnostic tools are employed to obtain detailed insights into the features of shock oscillations as well as communication of pressure fluctuations within the duct. The duct was not subject to an external back pressure and the inlet/isolator flow exhausted into the wind tunnel free stream.

2. Experimental set-up

2.1. *Test facility*

Experiments were conducted in the North Carolina State University variable Mach number blowdown type supersonic tunnel. The test section had a square cross-section of 150 mm $\times$ 150 mm and measured 650 mm in the streamwise direction. The wind tunnel can produce test section Mach numbers ranging from 1.5 to 4, although all tests in this paper were conducted at Mach 3.0. The total temperature, T_0, and total pressure, p_0, for these tests were 300 K and 618 kPa, respectively, leading to a free-stream static temperature, T_∞, pressure, p_∞, and velocity, u_∞, of 107 K, 16.8 kPa and 622 m s^{-1}. Fully established supersonic flow with these constant free-stream conditions can be maintained for approximately 8 s during a single test, allowing for the collection of both high and low frequency data.

2.2. *Experimental configuration*

A fully axisymmetric inlet/isolator with a constant area circular cross-section isolator ($D = 38.1$ mm) was used. The overall schematic of the test article can be seen in figure 1. The corresponding locations of the shock crossings and the static and pitot pressure probe placements are shown in figure 2. The test article consists of a steel inlet, a transparent isolator section made of acrylic comprising the entire measurement domain from $x/D = 3.67$ to $x/D = 9.00$ and a steel end section for the isolator. The steel inlet can be swapped out for different compression angles; in this paper we will predominantly look at the results obtained with a 10° compression angle. The contraction ratio, defined as the ratio between the inlet capture area to the isolator cross-sectional area, is 1.284. In all discussions, the x location is defined as the streamwise distance downstream of the inlet plane (defined as $x/D = 0$) and horizontal mid-plane of the isolator connects the azimuths $\phi = 0°$ and 180°.

For a limited set of experiments to delineate the upstream propagation length scale of acoustic information, an external shock wave was generated and located at a predetermined location by injecting a steady sonic jet as shown in figure 2. A circular jet injection port of diameter $0.126D$ was located at $x/D = 7.58$ and the sonic jet was injected normal to

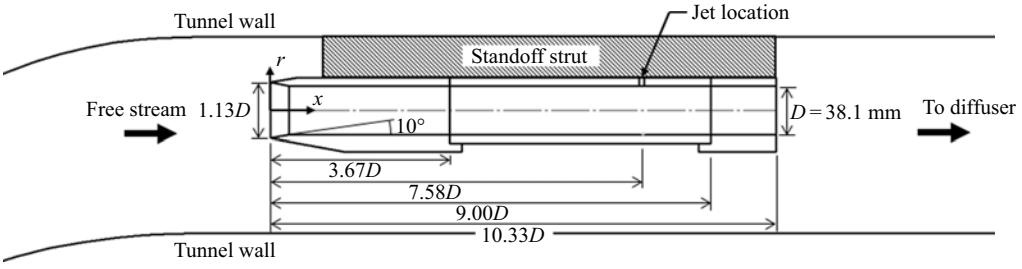

FIGURE 1. Axisymmetric inlet/isolator configuration as mounted within the wind tunnel with flow from left to right (dimensions normalised by the isolator diameter, D).

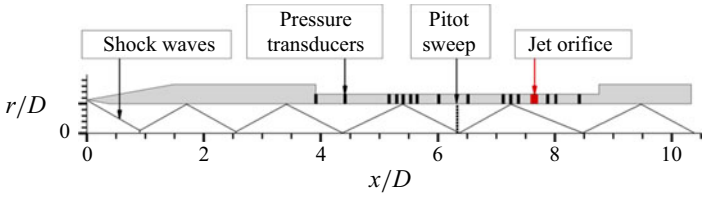

FIGURE 2. Experimental diagram of axisymmetric inlet/isolator with shock wave system sketch along with pressure transducer, Pitot probe and jet injection locations.

the streamwise direction. Compressed nitrogen was used for high-momentum sonic jet injection and the jet to isolator mass flow ratio was varied between 1.3 % and 6.6 %. A Peter Paul solenoid valve with a $0.063D$ orifice was used to precisely control the starting time of the jet and allows for a rapid rise in jet pressure. For a typical test run, the jet was injected for 5 s of steady mass discharge.

2.3. *Oil surface-streakline visualisation*

Streakline visualisation provides a qualitative measurement of surface shear stresses which is used to infer shock impingement locations, regions of separated flow, locations of flow reattachment and other surface features. The particular visualisation medium used here was a mixture of mineral oil and DayGlo Rocket Red pigment, which fluoresces red when subjected to UV light. The ratio of mineral oil to pigment used was dependent on how viscous the mixture needed to be to capture unsteady flow structures but also not be immediately removed from the regions of interest. A CMOS camera (Photron Inc., Model: Fastcam SA-X2) fitted with a Nikon f/1.2 50 mm lens acquired images of the isolator surface flow field at 60 Hz while an LED UV lamp (ISSI Inc., Model: LM2XLZ-400) provided a constant illumination throughout the test duration. The acrylic isolator section spanning $x/D = 3.67$ to 9.00 was imaged and the images were subsequently cropped to highlight certain flow regions within the isolator.

2.4. *Wall static pressure measurements*

2.4.1. *Point measurements using pressure transducers*

High frequency wall static pressure measurements using piezoelectric transducers were performed to provide pointwise quantification of the mean and fluctuating pressures along the isolator. Five piezoelectric ultra-miniature transduces (Kulite Inc., Model XCQ-062-15A) having a sensor effective frequency response of 200 kHz were utilised for

this purpose. The sensing membrane of the transducer was $0.019D$ in diameter; however, the protective screen on the top of sensing membrane rendered the effective sensing region to span $0.044D$ in diameter and reduced the effective frequency response of the sensor to 50 kHz. The signal from the pressure transducers were amplified $100\times$ using a low-noise amplifier (Vishay Model 2350) and then low-pass filtered (DL Instruments Inc., Model 4302A) with a cutoff frequency of 50 kHz. Lastly, an analogue-to-digital converter (NI Inc., Model: USB-6366) simultaneously sampled the signals at a rate of 500 kHz. At least 3 s of pressure data were recorded with fully established flow and constant stagnation conditions for each test and a selected 2 s interval was used for further analysis.

The Kulite pressure transducers were flush mounted to the isolator wall in the streamwise direction along $\phi = 0^\circ$. The transducer locations were clustered around regions of interest such as shock impingement locations and the boundary layer in the vicinity of the shock foot. The transducers were placed into custom housings to protect them and to allow them to be moved to different locations between tests. However, the custom housing limited the spacing between transducers to be a minimum of $0.12D$, which provided fine enough spatial resolution for unambiguous data interpretation.

An in-house MATLAB code using the following method was used to process the pressure data. First, the 2 s selected dataset was software low-pass filtered at 25 kHz. From this filtered dataset, mean, standard deviation and other basic statistical values were calculated for each transducer. Power spectral densities were calculated for each of the selected datasets using Welch's method of windowed Fourier transforms (Bendat & Piersol 1986) using 8 windows and a 50 % overlap which provided a good trade-off between reducing the variance of the periodogram and still providing an adequate frequency resolution of 3.8 Hz. Two-point cross-correlation coefficients and cross-coherences were calculated using built-in MATLAB functions.

2.4.2. *Pressure field imaging using high-speed pressure sensitive paints*

Two-dimensional pressure field was imaged using high-speed polymer ceramic pressure sensitive paints (PCPSP). The technique involves spraying a uniform coat of the PCPSP onto the isolator surface and illuminating the surface with a high power UV light source to excite the fluorescence of the paint. The paint fluoresces with a broadband emission centred at approximately 600 nm. In addition, the intensity of the emission is directly proportional to the local gas density, and hence the local pressure for a constant composition environment. A high-speed CMOS camera (Photron Inc., Model: SA-X2) fitted with a Nikon f/1.2 50 mm lens and a 590 nm long pass filter imaged the paint fluorescence at 8 kHz. Funderburk & Narayanaswamy (2019) recently validated the resulting PCPSP pressure data and the shock oscillation power spectra until 4 kHz using redundant pressure measurements from high frequency pressure transducers. The pressure field was imaged over one half of the circumference ($-90^\circ \leq \phi \leq 90^\circ$) and spanned $5.25D$ in the streamwise direction; however, the camera distortions along the edges necessitated using a sub-domain of the measurement area for further analysis.

2.5. *Planar laser scattering*

Planar laser scattering (PLS) was performed along the centre span of the model to obtain a semi-quantitative image of the shock structure within the isolator. The field of view extended between $x/D = 6.04$ and 7.74 and extended across the entire diameter of the isolator barring $\approx 0.1D$ above the isolator surface due to high surface scattering. Water vapour was introduced into the storage tanks of the wind tunnel before a test

and the amount of water vapour was controlled by the dew point of the dryer unit of the compressed air system. Some of this water vapour condensed to a droplet fog when accelerated to supersonic speeds within the wind tunnel as the static temperature attains very low values. The resulting fog density is related to the fluid density at any particular location within the flow. Hence, changes in density, such as across a shock wave, can be visualised by imaging the fog density. For example, regions with higher fluid density, such as just downstream of a shock, produces more laser scattering leading to high intensity counts in the PLS images. Conversely, areas with lower fluid density or higher temperatures produce less laser scattering and thus lower intensity counts. In a recent effort, Pickles *et al.* (2018) demonstrated a methodology to convert the PLS signal to gas density by accounting for the physical processes the particulates undergo in shock dominated flows. Higher temperatures such as within the boundary layer or downstream of strong shocks allow the condensed water to vaporise and drastically reduce the laser scattering in these regions lending these regions to be visualised with very high fidelity.

In this work, the laser illumination was produced from an Nd-YAG laser operating at 10 Hz with an output energy of $\approx$5 mJ per pulse and pulse width of $\approx$7 ns. The laser beam was frequency doubled to 532 nm and transformed into a 0.7 mm (0.018D) thick sheet with the focal point located at the centreline of the model and a Gaussian energy distribution along the sheet width. The sheet thickness, however, did not vary by more than 10 % across the entire imaging domain. Images of this illumination plane were captured by an interline CCD camera (PCO Inc., Model: Pixelfly) fitted with a Nikon f/1.2 50 mm lens and a 532 nm filter producing an spatial resolution of 7 μm pixel^{-1}. For each run, approximately 30 images were acquired during the fully started operation within the isolator region and the same configuration was tested multiple times to produce a larger dataset.

3. Results and discussion

3.1. *Inlet flow field characterisation*

A wall static pressure profile sweep along the entire isolator section was performed to quantify the flow development within the isolator section. Figures 3(*a*) and 3(*b*) show a comparison of the mean and root-mean-square (r.m.s.) pressure profiles measured along the isolator at $\phi = 0^\circ$ by transducers and a trace by the PCPSP; while figures 3(*c*) and 3(*d*) show the corresponding 2-D measurements using the PCPSP. No back pressure was introduced while making these measurements. For the point measurements, regions near shock impingement locations have a finer transducer spacing for more in-depth quantifications. The mean PCPSP wall static pressure field shown in figure 3(*c*) reveals four regions of high pressure of which three are also captured by the pressure transducers in figure 3(*a*). The pressure peaks correspond to where the inlet/isolator shock train impinge on the isolator surface and are followed by a gradual decrease in pressure due to the expansion fan that originate from the inlet shoulder. The azimuthal variation of pressure field at a given streamwise location exhibits a slightly higher value at the middle of frame ($\phi = 0^\circ$) compared to other locations. A part of this inflated pressure could be due to slight defocusing of the PCPSP signal in the region away from $\phi = 0^\circ$ and the extent of defocusing increases with increasing azimuthal offset from $\phi = 0^\circ$. Another possible source is non-uniform illumination per unit area due to the curvature of the test article leading to high azimuthal locations producing lower intensity signals and, to a similar effect, the self-view factor is highest along $\phi = 0^\circ$, increasing the intensity towards the centreline due to diffuse reflection of incoming illumination.

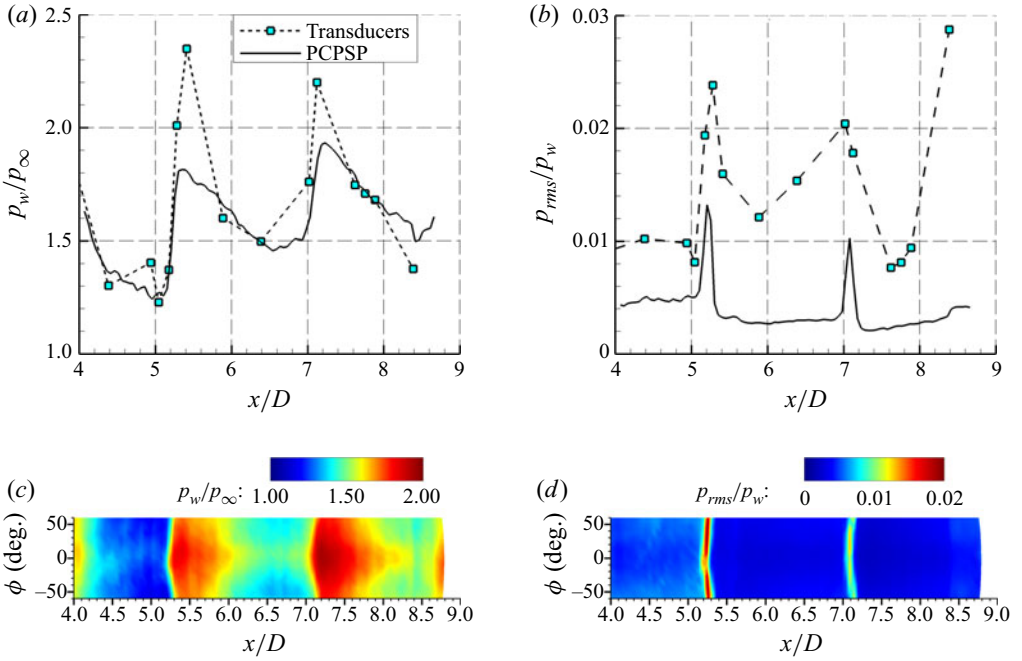

FIGURE 3. Mean and r.m.s. static pressure distribution along isolator wall. Comparison of Kulite transducer and extracted PCPSP trace at $\phi = 0^\circ$ for: (*a*) mean pressure; (*b*) r.m.s. pressure. Unwrapped PCPSP: (*c*) mean pressure field measurements; (*d*) r.m.s. pressure field measurements.

The corresponding unsteady pressure loading is shown as the wall-pressure normalised p_{rms} profiles in figure 3(*b*). Interestingly, both pressure transducer and PCPSP reveal only two peaks in the p_{rms}, which contrasts the four regions of high pressure observed in the mean PCPSP measurements shown in figure 3(*c*). The absence of the other two possible peaks (at $x/D \approx 4$ and $x/D \approx 8.8$) from the PCPSP is because the PCPSP measurement domain excludes the peak shock loading locations in the most upstream and most downstream shock legs. As one traverses across any individual shock foot, the normalised p_{rms} increased from approximately 0.01 in the boundary layer to 0.03 beneath the shock foot. The normalised p_{rms} observed from the PCPSP measurements is slightly depreciated because the maximum frequency that is resolved by the PCPSP is 4 kHz, compared to 25 kHz by Kulite pressure transducers. Despite this, the bands of elevated normalised p_{rms} that indicate the shock foot maintains a consistent value across the azimuthal direction, show a maximum end-to-end deviation of less than $0.13D$ in the streamwise direction, and agree with the streamwise peak locations from transducer data. Furthermore, the streamwise extent of the elevated normalised p_{rms} corresponds to the length scale of shock oscillations. Figure 3(*d*) reveals that both of the shock feet imaged by the PCPSP oscillate over a distance of $0.13D$. For the subsequent discussions, we consider only the two shock legs that intersect the isolator surface at $x/D = 5.38$ and 7.22. Furthermore, the shock impingement located at $x/D = 5.38$ will be referenced as the 'upstream shock leg' and the shock impingement located at $x/D = 7.22$ will be referenced as the 'downstream shock leg'.

The fractional rise in pressure due to the individual shock legs on the isolator surface was compared with the empirical inviscid pressure ratio determined by Korkegi (1975)

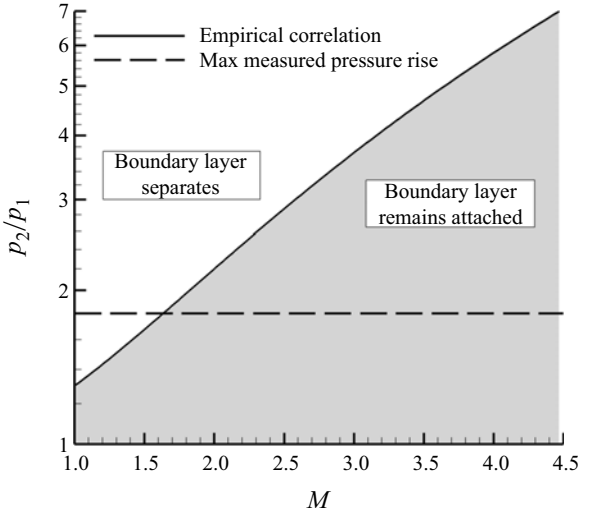

FIGURE 4. Empirical relation for the required pressure rise across the shock wave in order to cause separation of a turbulent boundary layer as compared with the maximum recorded pressure rise.

for incipient separation onset. It should be noted that the wall pressure takes a longer development length downstream of the shock due to viscous effects and the values are typically depressed compared to the inviscid pressure rise. However, it can be argued that the peak pressure obtained in the downstream vicinity of the shock is still very close to the inviscid pressure rise, thereby justifying the comparison within a certain margin. For the free-stream Mach number of 3.0 implemented here, the Korkegi criterion suggests a pressure rise of 3.7 times across a shock is necessary to separate a turbulent boundary layer but this is not a hard requirement in this experiment configuration as the local 'free-stream' Mach number should be less than 3.0 everywhere within the isolator due to processing by the inlet shock waves. The upstream shock leg (located at $x/D = 5.38$) indicates a pressure ratio of 1.8 times, while the downstream shock leg (located at $x/D = 7.22$) indicates a pressure ratio of 1.5. Both these values are well below the limit calculated for Mach 3.0 and it can also be seen in figure 4 that the Mach number would have to reduce to below 1.6 for the given shock strengths to cause separation, suggesting that the mean flow should remain attached across both of these shock impingement locations. Furthermore, the mean surface-streakline field and PLS plane in figure 5 also evidence the lack of mean separation, and the r.m.s. of the PLS fields (not shown) evidences the absence of any instantaneous separation that may be observed with incipient separation conditions. Thus, the shock interactions with the isolator boundary layer do not generate either mean or instantaneous boundary layer separation.

The velocity profile within the inlet/isolator was obtained using Pitot pressure sweeps to establish the extent of symmetry in the flow field as well as to provide a determination of the boundary layer thickness at the measurement station. The measurement station was chosen to be $x/D = 6.30$ which lies in between the upstream and downstream isolator shock legs. Figure 6(a) shows the mean velocity profile near the wall at the measurement station, where each velocity value was averaged over 10 000 highly repeatable data samples. The nearest location to the isolator wall with reliable data was $0.013D$; this offset resulted in only the outer part of the boundary layer being resolvable. It can be observed

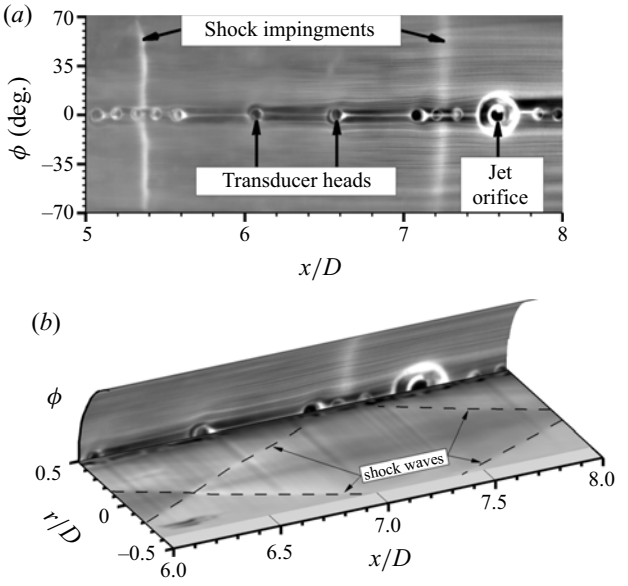

FIGURE 5. Flow visualisation of the isolator in the clean flow configuration (no jet injection): (*a*) mean unwrapped full field-of-view surface-streakline field; (*b*) combination mean PLS along the r/D axis and surface-streakline images wrapped on a constant $r/D = 0.5$ surface.

from figure 6(*a*) that the 'free-stream' velocity at the measurement station was $\approx 0.95u_\infty$. The velocity profile decreases to 99 % of the local free-stream value at approximately $0.11D$ from the isolator wall and the velocity drops to 78 % of the local free-stream value at the smallest measurable distance from the wall. This profile provides estimates of the boundary layer thickness, displacement thickness and momentum thickness of $\delta_{99\,\%}/D = 0.113$, $\delta^*/D = 0.048$ and $\theta/D = 0.0081$, respectively, and the 2-D cross-sectional fraction of viscous region at 0.213. The Pitot pressure profile shown in figure 6(*b*) is fairly symmetric about the model centreline. A deficit in Pitot pressure can be observed in the vicinity of the centreline most probably resulting from a Mach reflection within the upstream, unviewable domain and, as expected close to the wall, the Pitot pressure monotonically decreases within the boundary layer due to viscous dissipation. Overall, a fair amount of mean flow field symmetry can be observed about the model centreline.

3.2. *Power spectrum evolution across the isolator channel length*

The power spectral densities (PSDs) of wall-pressure fluctuations at various streamwise locations were calculated to investigate the energy content of the self-sustained shock oscillations and the boundary layer before and after getting processed by the shock wave. PSDs with and without frequency pre-multiplication will be shown as each has unique insights into the harmonic nature of the pressure signal. Non-premultiplied PSDs are the Fourier transform of the autocorrelation and thus can be thought of as the energy within a frequency bandwidth for a single period of oscillation. This representation is useful in telling the quantity a frequency band contributes to the fluctuations of the original signal. Going off of this, the premultiplied PSDs represent the same energy within a frequency bandwidth but over a set period of time rather than the individual period of oscillation.

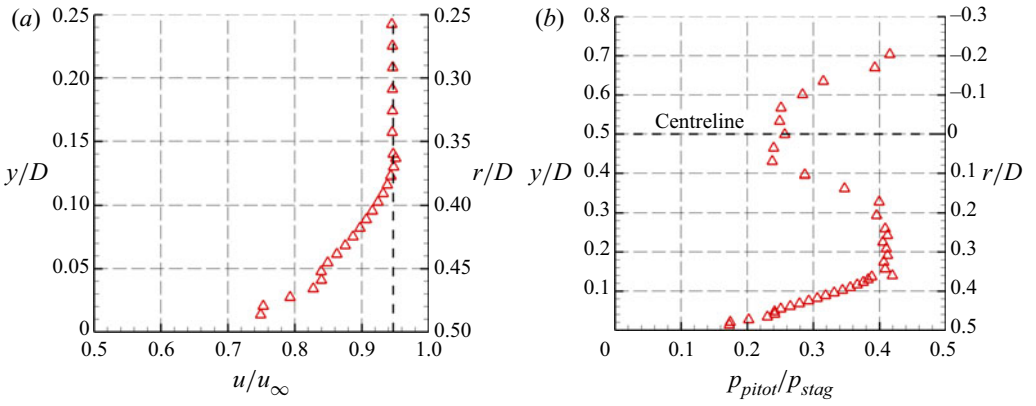

FIGURE 6. Velocity and Pitot pressure profiles across the isolator at $x/D = 6.33$: (*a*) velocity profile; (*b*) ratio between Pitot pressure and stagnation pressure of free stream.

This representation is better at displaying which frequency bands contribute the most total energy in the original signal.

Figure 7(*a*) shows the frequency pre-multiplied PSD of the incoming boundary layer that interacts with the upstream shock leg measured at $x/D = 5.14$, which is located $0.24D$ upstream of the shock impingement location. Figure 7(*a*) shows that the boundary layer contains a broad range of frequencies that span several decades and the frequency-multiplied PSD exhibits a monotonic increase with frequency over the range measured. This trend is consistent with classical turbulent boundary layer spectrum where the peak energy is located at the boundary layer convection frequencies (u_∞/δ). From this point on, frequencies will be normalised with respect to the characteristic duct frequency based on flow through time, $f_c = u_\infty/L$ (where L is the duct length), which is 1580 Hz. This characteristic frequency based on the duct length is typically used for acoustic interactions occurring over a significant length of a duct. Notably, however, interactions that only pertain to a single shock interaction will typically use a boundary length scale instead. Considering that previous literature has demonstrated strong acoustic interactions within the duct, it was decided to use the duct characteristic frequency as the normalising parameter. In the present flow, the peak from boundary layer convection lies in the excess of $63f_c$, which is greater than the maximum measurable frequency of the transducers utilised in this study.

The frequency pre-multiplied PSD wall-pressure fluctuations beneath the upstream shock leg ($x/D = 5.38$) and the downstream shock leg ($x/D = 7.22$) are presented in figure 7(*b*). Interestingly, the PSDs beneath both shock foot locations show broadband elevated values between $0.006f_c$ and $0.32f_c$, with a peak magnitude occurring at around $0.032f_c$, significantly below the characteristic frequency based on either the duct or boundary layer length scales. This low frequency bump is followed by a trough until there is a steep and continuous increase up until the maximum measurable frequency of $15.8f_c$. This steep increase in PSD with frequency is quite suggestive of the incoming turbulent boundary layer fluctuations that is persistent through the shock wave. Finally, the sharp spikes at around $0.9f_c$ were inconsistent in magnitude across all datasets for an unknown reason. For a majority of the tests, these spikes were not prominent enough to be considered significant while they were dominant features in a few tests. At first, it was believed that these spikes were not due to the flow itself but some outside source

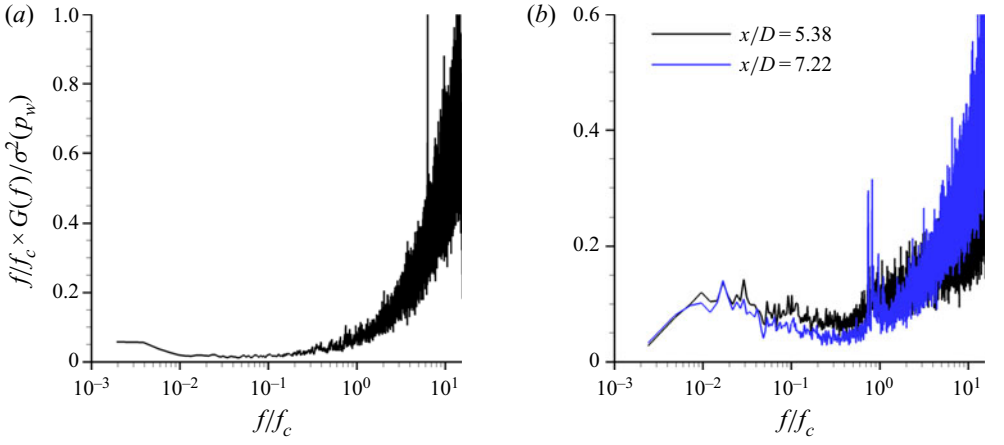

FIGURE 7. Frequency pre-multiplied pressure spectral density of wall-pressure fluctuations measured beneath (*a*) boundary layer at $x/D = 5.14$ located $0.24D$ upstream of the upstream shock leg; (*b*) upstream and downstream isolator shock legs.

but upon further inspection, via averaging only across tests which did not contain an appreciable peak, it appears it is caused by sources related to wind tunnel vibrations or some other aerodynamic sources. As such, it is not possible to ascertain the cause of these spikes. Not shown is a comparison of the non-normalised PSD magnitudes (dimensional analogue of figure 7*b*) which revealed the downstream shock leg contains substantially higher energy frequency content compared to upstream shock leg oscillations. However, this difference can easily be attributed to numerous sources, such as the difference in the relative proximity of the transducer to the respective mean shock foot positions, spatial amplitude of the shock oscillation and the shock strength.

The power spectral density of the boundary layer that is processed by the shock wave and its subsequent downstream evolution is analysed to learn if any of the low frequency humps in the shock oscillations have their origin in the downstream boundary layer. For comparison, the PSD of the incoming boundary layer to the shock leg and the PSD beneath the shock foot are also presented. Figures 8(*a*) and 8(*b*) show the PSD of the incoming boundary layer (measured $0.13D$ upstream of the mean shock foot location), shock foot oscillations and the relaxing boundary layer (measured $0.13D$ downstream of the mean shock foot location) for the upstream and downstream shock legs, respectively. The power spectrum without frequency pre-multiplication is presented to highlight the changes in PSD across all frequencies. The red, blue and black curves in both figures represent the incoming boundary layer, relaxing boundary layer just downstream of the shock and the shock foot locations, respectively. Comparing the PSD of the incoming and relaxing boundary layer for a given shock foot, it can be observed that the relaxing boundary layer has noticeably higher energies at frequencies exceeding $10f_c$, while the mid-frequencies contain similar values. To provide a context on the relative strength of PSD at different frequencies, the PSD of the relaxing boundary layer between $0.06f_c$ and $6.33f_c$ exhibits an amplitude of approximately 5 % of the peak measured at $0.006f_c$. The corresponding PSD for the incoming boundary layers compared to the shock oscillation is at least an order of magnitude lower. Beyond $6.33f_c$, both the incoming boundary layer and the relaxing boundary layer exhibit a similar magnitude uptick in their PSD. From the non-normalised PSD, the important difference in the relaxing boundary layer is an order of magnitude

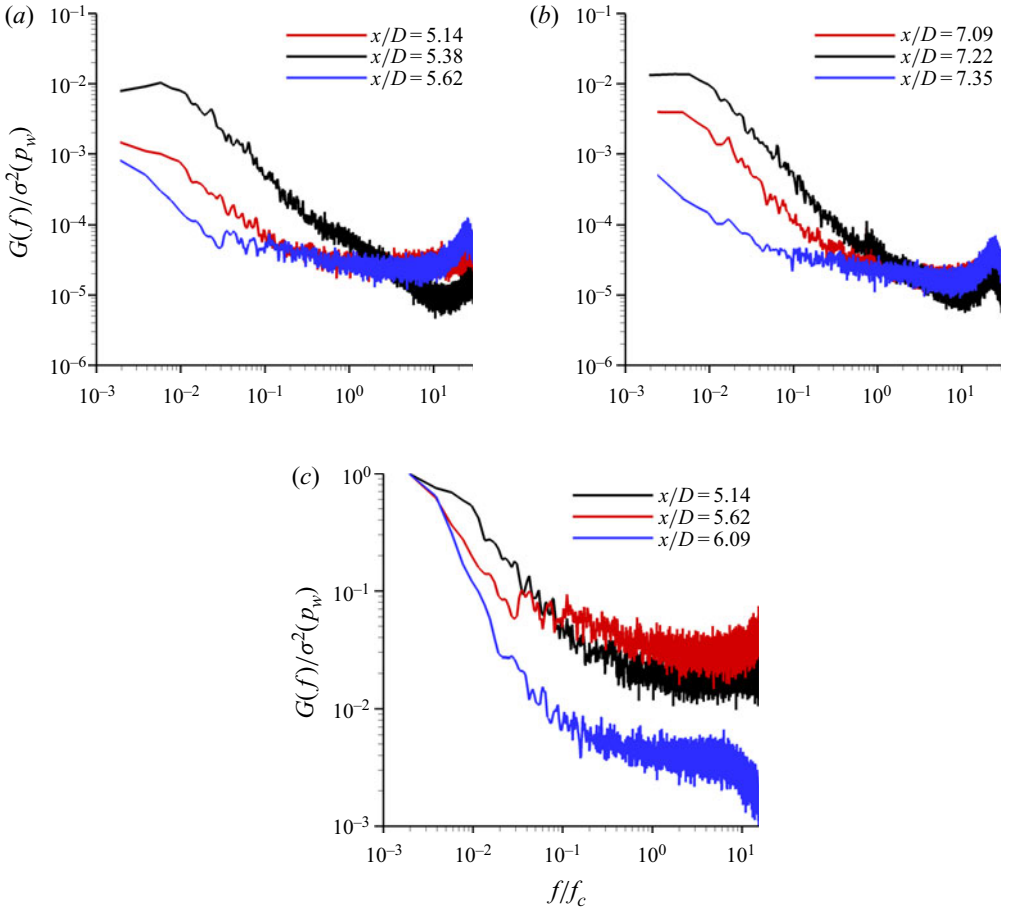

FIGURE 8. Power spectral densities of wall-pressure fluctuations measured: (*a*) in the vicinity of upstream shock isolator impingement location; (*b*) downstream isolator shock impingement location; (*c*) at locations before and after upstream isolator shock impingement location.

increased energy at the intermediate frequency between $0.06f_c$ and $6.33f_c$ compared to the incoming boundary layer.

The evolution of the PSD of the relaxing boundary layer processed by the upstream shock leg is shown in figure 8(*c*), normalised here by the peak energy as this best illustrates the relative strength of the PSD at higher frequencies. The PSD of the canonical turbulent boundary layer that is incident on the upstream shock leg is also presented in figure 8(*c*) for comparison. It can be observed from figure 8(*c*) that the elevated strength at the intermediate frequencies greater than $0.06f_c$ is carried over a considerable streamwise distance. For example, the PSD at $x/D = 6.09$ ($0.71D$ or 6.3δ downstream of the shock foot) shows that the normalised energy content at frequencies greater than $0.06f_c$ lies in between those at $x/D = 5.62$ and the canonical turbulent boundary layer (measured at $x/D = 5.14$). The gradual dissipation of the high frequency continues with downstream distance, and by the time the downstream shock leg is encountered, the boundary layer has almost recovered to the canonical PSD distribution, as shown in the PSD of $x/D = 7.09$ location in figure 8(*b*). Figure 8(*b*) also exhibits an interesting uptick in the energy content by approximately five times at low frequencies ($<0.06f_c$) for the boundary layer incident on

the downstream shock leg ($x/D = 7.09$) compared to the boundary layer incident on the upstream shock leg ($x/D = 5.14$), which may suggest some degree of back scattering in the boundary layer frequencies during the relaxation process. However, it should be noted that the PCPSP-based pressure field imaging shows that $x/D = 7.09$ lies at the upstream periphery of the p_{rms} inflation associated with the downstream shock foot (figure 3*d*), which suggests the shock motion extends to $x/D = 7.09$. Hence, the strengthening of low frequency pressure fluctuations at $x/D = 7.09$ could be simply an artefact of intermittent shock foot presence. Although not presented, a very similar downstream evolution was also exhibited by the relaxing boundary layer generated by the downstream shock leg.

3.3. *Communication between and within a shock wave impingement location*

The discussions presented thus far show that there is a clear difference in the PSD of shock foot oscillations for the inlet/isolator when compared to the shock oscillations with 2-D SBLI units with shock-induced separation, where the shock oscillations are governed by the separated flow pulsations. Interestingly, the very low frequencies of shock oscillations in unseparated SBLI cannot be directly traced to either the incoming or relaxing boundary layer. Very few works so far have investigated the unseparated shock oscillations and none of them have made direct wall-pressure measurements. Notable among the relevant works include that of Smits & Muck (1987) who performed hot-wire measurements of unseparated compression ramp interactions at various wall-normal locations starting from $y/\delta = 0.2$. The authors noted that the turbulent mass flux PSD in the near-wall locations of an attached compression ramp interaction exhibited no noticeable spectral peaks at the low frequency range ($\approx$100 Hz) and the overall spectrum resembles that of the incoming boundary layer PSD due to turbulence-induced jitter on the shock oscillations. It is not clear if a direct measurement of the shock oscillations using wall-pressure measurements would have revealed low frequency range oscillations in that study as well.

It should be remarked that the low frequency shock oscillation peaks were reported in the external and internal flows with shock-induced separation wherein the back pressure fluctuations as well as the separated flow pulsations provided the low frequency content to the shock oscillations. Considering there is no boundary layer separation in the flow field considered in the present study, to the authors' knowledge, this is the first study to document these very low frequency oscillations in unseparated flows. Such low frequency shock oscillations can potentially couple with structural resonances or cause hot spots within the ducts, and hence would necessitate additional aero-structural considerations during design.

Of particular interest is what causes the low frequency shock oscillations in these unseparated internal flows. While there are several studies that provide detailed insights into the upstream propagation of pressure fluctuations in separated flows (discussed in § 1), the issues with extending these ideas to unseparated flow of the current study include: (i) the lack of flow separation in the current inlet/isolator flow field cannot seed the shock oscillations with low frequencies associated with separated flow pulsations; and (ii) the sonic line is estimated to lie well within one millimetre from the isolator wall ($<0.03D$) based on the boundary layer profile presented in figure 6(*a*), and these near-wall regions are expected to have very high shear and appreciable viscous forces. The latter two factors are expected to cause significant damping and dispersion effects to the upstream propagating acoustic waves in the subsonic region of the boundary layer. It is not clear how far the pressure perturbations can travel upstream in these non-canonical relaxing boundary layers. Hence, to unravel the driving mechanisms of the shock oscillations, we

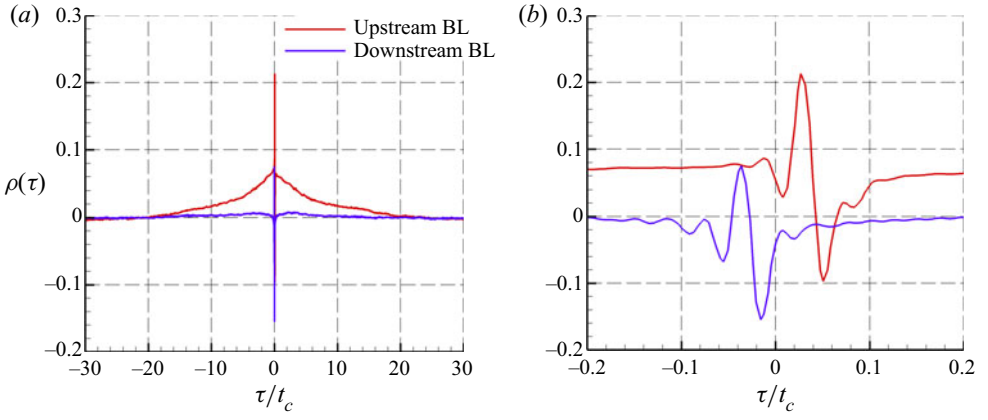

FIGURE 9. Cross-correlation coefficient between upstream isolator shock impingement location and boundary layer in the upstream and downstream vicinity of the shock foot with the reference transducer beneath the shock foot across: (*a*) a wideband time delay; (*b*) a narrowband time delay.

need to first answer if the oscillations arise because of global interactions across the duct length or due to local interactions around the shock foot. Hence, the subsequent discussions will help pin down the communication mechanisms and length scales of the downstream and upstream propagations of the pressure fluctuations that originate within the isolator channel.

3.4. *Downstream communication through the isolator channel*

Knowing how the upstream and downstream shock legs influence each other's dynamics is next in unfolding the dynamics of the isolator system. Two-point cross-correlations are extremely useful in determining information propagation directions and speeds and thus was the method of choice in this study. For all cross-correlation plots, the pressure trace from a transducer underneath a shock leg was taken as the stationary function, p_1, and the pressure trace from other correlating location was the sliding function, p_2. Thus, a positive (negative) lag at a cross-correlation extremum indicates that the sliding pressure signal pressure trace, p_2, is leading (lagging) the reference transducer location, p_1. Figure 9 shows the two-point cross-correlations between the pressure fluctuation emanating from the upstream shock leg and the incoming boundary layer, measured $0.24D$ upstream of the shock leg. Two clear features are observable in the correlation plots: sharp extrema that are located at very small time-lag values, and a smooth broader region of decreasing correlation magnitude that extends along both positive and negative time lags. As the transducer that is located beneath the shock leg is the reference in the cross-correlation calculation, the positive time lag corresponding to the sharp maxima shows that the fluctuations in the incoming boundary layer leads the shock fluctuations. This time lag is converted to a corresponding velocity by using the simple ratio of the distance between the measurement points to the time lag, $u = \Delta x/\tau$, and gives an approximate speed of downstream propagation of $0.87u_\infty$, which is very close to the boundary layer convection velocity. The relatively modest value of the correlation peak suggests that the shock fluctuations have a small but non-trivial influence from the downstream convection of the turbulent boundary layer structures.

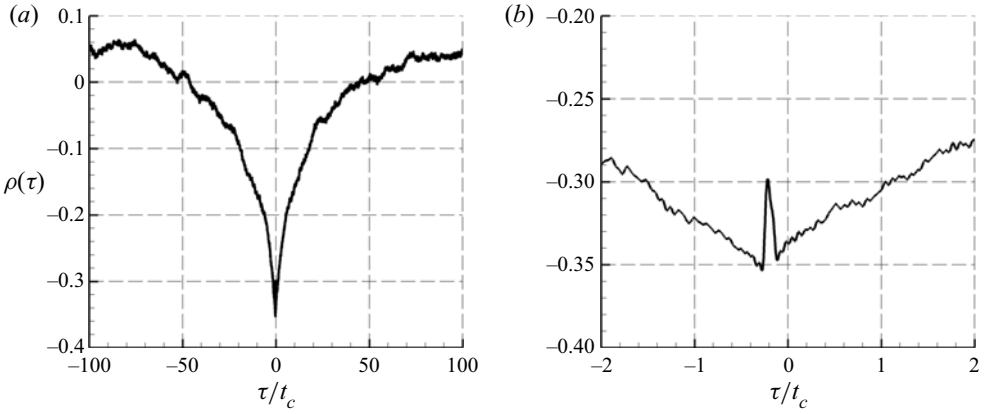

FIGURE 10. Two-point cross-correlation coefficient between the pressure fluctuations at the upstream and downstream shock impingement locations with the upstream shock impingement location as the reference transducer across: (*a*) a wideband time delay; (*b*) a narrowband time delay.

Similarly, the two-point correlation between the shock foot and downstream boundary layer reveals that the shock foot fluctuations lead the downstream boundary layer fluctuations with a similar propagation speed as the boundary layer structures. This suggests that the correlation occurs from the amplification of the boundary layer turbulence across the shock wave. Interestingly, the broad decay in the correlation observed with the incoming boundary layer is absent with the relaxing boundary layer. Once again, the cross-correlation magnitudes are quite modest, suggesting a weak contribution from the shock processing on the downstream boundary layer.

The two-point cross-correlations between the upstream and downstream shock leg are next considered and presented in figure 10. A strong negative correlation with negative time lag at the correlation peak is observed. The negative time-lag peak signifies that the upstream shock leg pressure fluctuations lead the downstream shock leg fluctuations. Once again, the time lag of the peak correlation was converted to the corresponding velocity of the pressure fluctuation propagation, which stood at $0.82u_\infty$. Once again, this value being very close to the boundary layer convection velocity strongly suggests that the communication of the perturbations between shock legs occurs through the boundary layer structure convection. In other words, the fluctuations introduced by the upstream shock foot on the boundary layer convects along the isolator and elicits a corresponding response from the downstream shock foot.

The broad spread of the cross-correlation between the shock legs over large time lags, observed in figure 10, suggests a wide range of shock oscillation frequencies are correlated. Hence, it is important to learn which oscillation frequencies are best correlated and communicated across. The coherence spectrum provides this piece of information as it forms the spectral analogue of the cross-correlations. A calculated coherence of unity represents a linearly coupled system, whereas a value of zero would represent uncoupled system and, unlike the cross-correlation, is not dependent on which pressure signal is considered the reference. Figure 11 shows the magnitude squared coherence between the upstream and downstream shock legs over the measured frequency range. A very high coupling ($C_{xy}(f/f_c) \geq 0.4$) in the shock oscillations are observed at the low frequencies of interest ($f/f_c < 0.10$) and the values approach zero at high frequencies representative

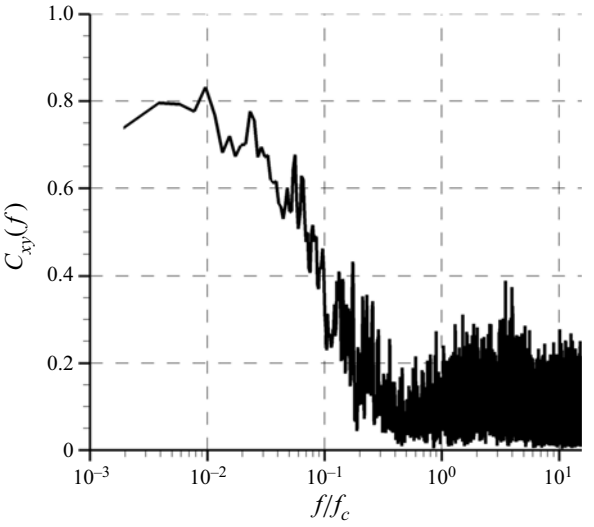

FIGURE 11. Two-point cross-coherence of pressure traces between the upstream and downstream shock impingement locations to illustrate the shock oscillation coupling at different frequencies.

of shock jitter. This shows that the propagation of perturbations between the shock legs through boundary layer convection indeed provides the downstream coupling channel for low frequency shock oscillations. While it was not presented here, essentially identical findings were also obtained with the other isolator configurations that were tested with changing isolator diameter and inlet angle. Summarily, the downstream propagation of pressure fluctuations at low frequencies of interest occurs over large streamwise distances via boundary layer convection.

3.5. *Upstream communication through the isolator duct*

The upstream propagation of pressure fluctuations in the isolator duct with shock-induced flow separation was shown to occur via acoustic propagation through large subsonic regions, either via a thick boundary layer or highly separated regions (Hunt & Gamba 2019). While the previous studies have shown that such propagation can extend across the entire isolator length, largely facilitated by the broad subsonic regions within the duct, it is not very clear how long such propagation can occur with unseparated, thin boundary layers. Previous studies used theoretical analyses to show the upstream propagation of acoustic waves within a canonical supersonic turbulent boundary occur over a length scale of local boundary layer thickness (Ramesh & Tannehill 2004; Miller 2018). However, boundary layers that get processed by the shock exhibit significant deviation in their structure and dynamics and it is not clear whether the upstream propagation distances are still maintained.

Experimentally unravelling the acoustic propagation length scales in unseparated flows is challenged by the very small acoustic pressure fluctuation amplitudes, anticipated dissipation of these waves by viscous forces with distance and the limitation in the spacing of the transducers within close distance and the sensitivity of PCPSP measurements. All these factors would substantially diminish the magnitude of the statistical correlations and coherences for making meaningful inferences unless one has an estimate of the length

scales over which acoustic propagation occurs prior to making cross-correlation studies. Hence, the approach undertaken here is to first demonstrate the length scale of upstream acoustic propagation from an alternate setting.

The alternate setting comprises of having two independent shocks within the isolator and observing what separation between the shocks would cause the upstream shock to respond to the presence of the downstream shock. The experimental set-up to create this situation consists of injecting a sonic jet into the isolator, which creates a jet shock system that could be placed at predetermined downstream distances from the isolator downstream shock foot. Having a jet shock creates strong perturbations to the isolator shock train that will help make meaningful measurements. During the experiments, the isolator shock leg locations were fixed since the inflow conditions and inlet geometry remained unchanged, and the jet port location was always at $x/D = 7.58$ ($0.37D$ or 3.3δ downstream of the undisturbed isolator downstream shock leg). The mass flow rate of the jet is varied to change the jet separation shock location over $x/D = 7.48$ ($0.26D$ downstream of the isolator downstream shock leg) all the way to physically merging with the isolator downstream shock leg. The effect of having different strength jets on the shock oscillations is quantified by investigating the PSD of pressure fluctuations beneath the upstream and downstream shock leg.

First, the impact of the jet injection on the isolator upstream shock leg, which is separated from the jet separation shock by a streamwise distance of $2.10D$ to $2.62D$ or approximately 16δ to 20δ depending on the jet strength, is investigated. Figure 12 presents the calculated PSDs at the two isolator shock foot locations without and with mass injection, where the jet strength is quantified by the ratio of the mass flow rates between the jet and isolator flow from the inlet capture. Each PSD presented is an average of three highly repeatable test runs of 10^6 data points (2 s) for each run. The range of injection strength implemented here provides an examination of the upstream shock leg under two situations: first, when the jet shock is located far enough downstream of the isolator downstream shock leg that there is little to no modification in its unsteady characteristics ($\dot{m}_{jet}/\dot{m}_{iso} < 5.2\,\%$), and the second when there is a considerable modification of the mean and unsteady characteristics of the isolator downstream shock leg ($\dot{m}_{jet}/\dot{m}_{iso} \geq 5.2\,\%$) due to physical merging, as will be seen later. It should be noted that the isolator downstream shock leg after physical merging with the strongest jet shock is located approximately 16δ downstream of the upstream shock leg. It can be observed from figure 12(a) that the jet injection of various strengths did not cause any appreciable qualitative or quantitative change in the upstream shock leg oscillation PSD. This indicates that perturbations caused both by the jet injection and gross modification to the downstream shock leg are not felt at the upstream shock foot location, signifying that the acoustic pressure fluctuations cannot propagate $O(10)$ boundary layer thicknesses upstream. It should also be noted that, whereas only shock oscillation information is shown here, the observed mean wall pressure as well as r.m.s. and other higher-order statistics of the pressure fluctuations did not exhibit any statistically significant changes either.

Having established a first upper bound of upstream acoustic propagation at $O(10)$ boundary layer thickness, a further refinement is obtained by examining the isolator downstream shock leg oscillation response to the jet injection. In this situation, the mean jet shock is located between $0.26D$ (2.3δ) and $0D$ (physical merging) from the downstream shock leg. At this close proximity range, it is important to consider the jet separation shock oscillation that can cause instantaneous physical merging with the isolator downstream shock leg, which may be wrongly attributed to acoustic propagation. To obtain an upstream extent of the jet separation shock motion, the r.m.s. of the PLS fields was computed and a threshold value of 20 % above the inviscid core region

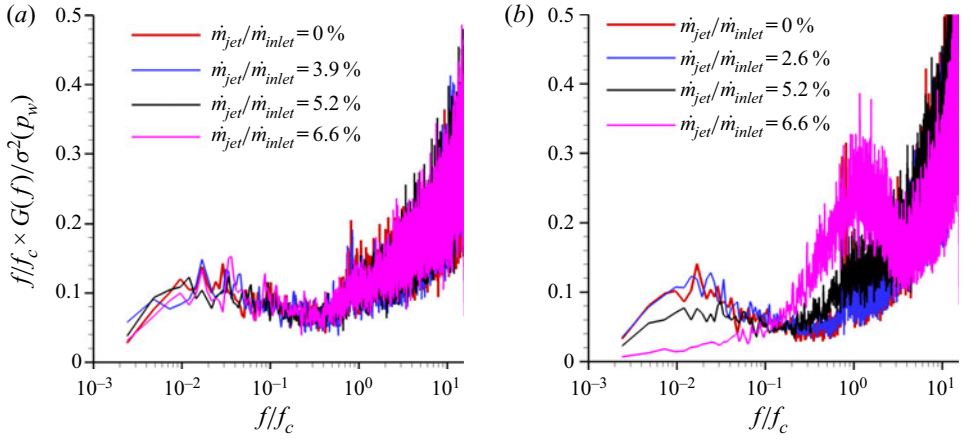

FIGURE 12. Frequency-multiplied PSD underneath shock impingement locations with various jet mass injection strengths: (*a*) upstream shock impingement location; (*b*) downstream shock impingement location.

r.m.s. was chosen to delineate the upstream extent of separation shock motion at a given wall-normal distance. This was extrapolated to the isolator wall to obtain an estimate of the upstream location of jet separation shock foot motion. As a redundant measurement, the surface-streakline images shown in figure 13 were analysed to provide the location of the mean upstream influence line, which again estimates the upstream travel of the jet separation shock. A more concrete determination of the region of jet separation shock motion was also made using unsteady wall-pressure measurements. Despite these redundant measurements, one should exercise abundant caution during data interpretation since the weak compression waves that emanate from the separation shock within the boundary layers are hard to capture using PLS or streakline visualisation, which causes the PLS and streakline fields to underestimate the upstream jet separation shock motion amplitude. The wall-pressure data also have a spatial resolution limitation of $0.12D$ that precludes an exact determination of the upstream extent of shock motion. However, the closest upstream location to the jet separation shock where the pressure signal ceases to exhibit the low frequency shock unsteadiness characteristic of separation shock oscillations will help estimate an upstream bound of the jet separation shock motion.

Figure 14 compiles the surface-streakline visualisation field, along with the PSD comparison at the isolator downstream shock leg location with and without jet injection, and centreplane mean and r.m.s. PLS fields around the isolator downstream shock leg and jet separation shock for a single jet strength. The jet injection employed here had the lowest strength among those tested ($\dot{m}_{jet}/\dot{m}_{iso} = 1.3\,\%$). The mean PLS field shows that jet separation shock foot is located at approximately $x/D = 7.48$, while the r.m.s. of the PLS field shows that shock foot fluctuations become appreciable at $x/D \approx 7.45$, which provides an estimate of the upstream extent of jet separation shock motion. This estimated upstream extent is also consistent with the upstream influence location determined from the surface-streakline visualisation. In addition, the pressure signal at $x/D = 7.32$ (not shown) did not possess any low frequency unsteadiness from the jet separation shock. This places the jet separation shock location at $x/D = 7.45$, which is approximately 2.1δ downstream of the isolator downstream shock leg. With this jet separation shock location,

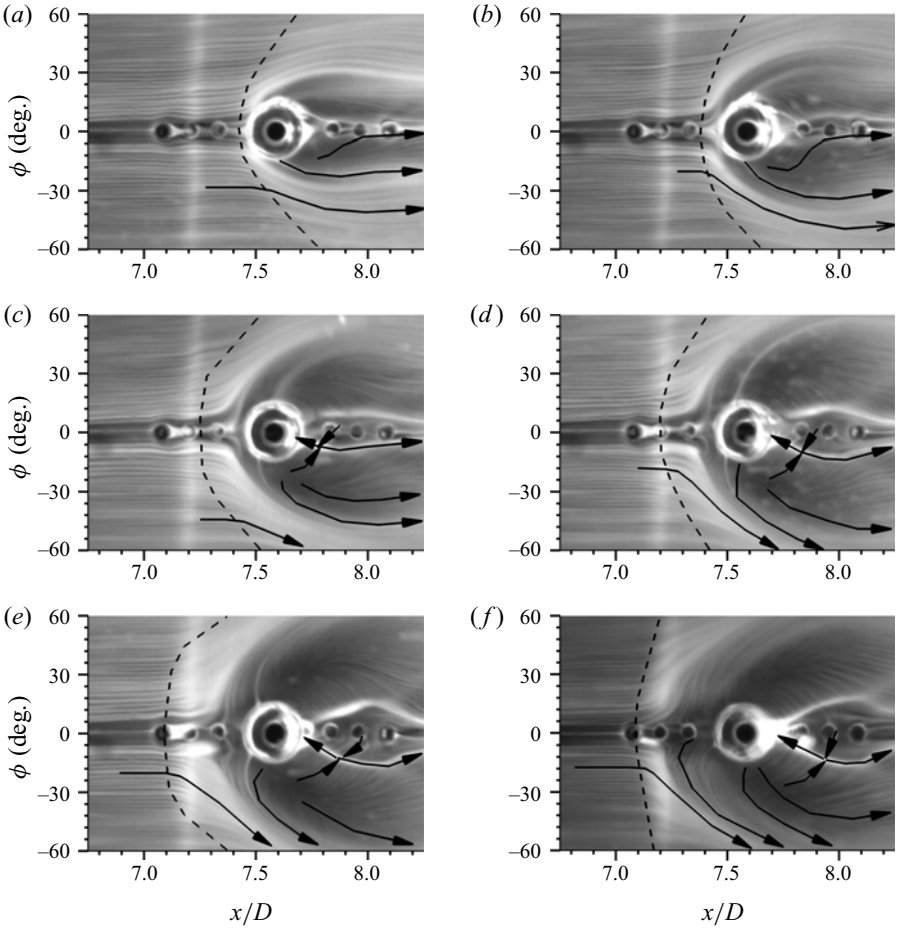

FIGURE 13. Mean surface-streakline visualisation fields with sonic jet injection of mass ratios $\dot{m}_{jet}/\dot{m}_{iso}$ of: (*a*) 1.3 %; (*b*) 2.6 %; (*c*) 3.9 %; (*d*) 5.2 %; (*e*) 6.6 %; (*f*) 7.8 %. Dashed lines indicate where streaklines begin to deviate from the clean flow configuration while solid lines with arrows indicate streakline direction. Streaklines are symmetric approximately $\phi = 0^\circ$ so only the lower half is marked with lines.

the PSD of the isolator downstream shock leg oscillations (figure 14*b*) reveals no identifiable qualitative or quantitative changes compared to the situation without jet injection. This observation shows that a revised upper bound of the upstream propagation of the perturbation occurs at 2.1δ, which is an order of magnitude smaller than the previous estimate made using the upstream shock response. This length scale of $O(\delta)$ is also essentially identical to the estimates provided with canonical boundary layers, which serves to show that the relaxing boundary layer did not significantly augment or inhibit upstream acoustic propagation.

3.6. *Physical model of shock oscillation mechanism and implications for inlet unstart*

From the insights into the propagation of perturbations across the isolator duct, it is clear that the isolator shock foot oscillations have contributions from downstream travelling boundary layer structures (exhibiting diminishing correlations with distance) and upstream

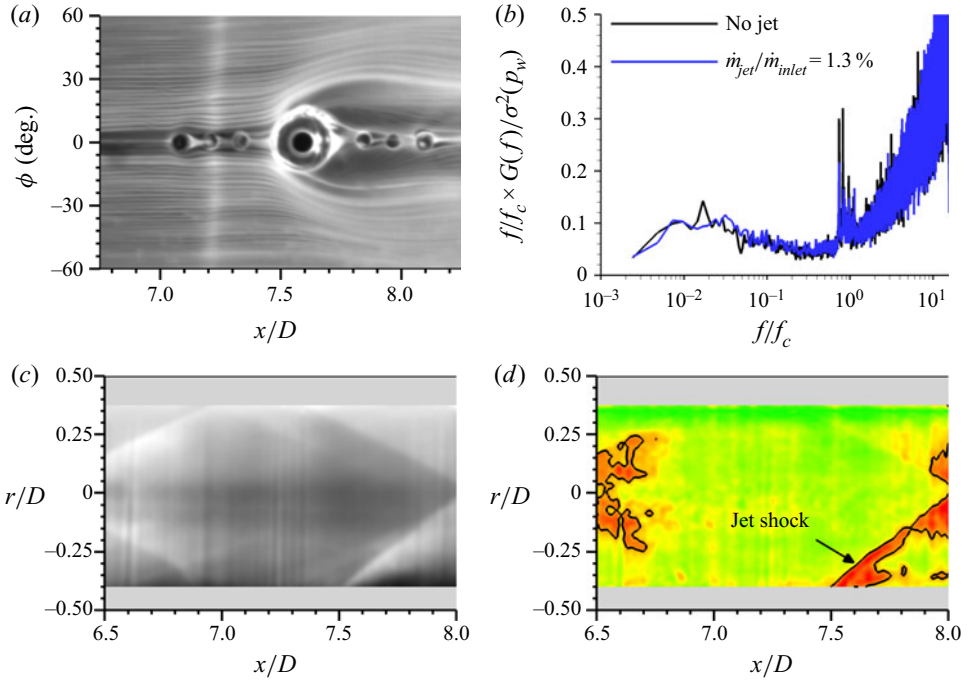

FIGURE 14. Isolator flow and pressure field with sonic jet injection of mass ratio $\dot{m}_{jet}/\dot{m}_{iso} = 1.3\,\%$: (*a*) mean surface-streakline visualisation field; (*b*) comparison frequency pre-multiplied PSD of wall-pressure fluctuations measured beneath the isolator downstream shock foot ($x/D = 7.22$) with and without jet injection; (*c*) corresponding mean PLS field with jet injection; (*d*) corresponding r.m.s. PLS field.

propagating acoustic pressure fluctuations within an order of one boundary layer thickness proximity, as illustrated by the schematic in figure 15. These provide compelling evidence that the isolator shock foot oscillations typically occur from local interactions with the surrounding boundary layers and have very little response from the 'global' back pressure fluctuations of the duct. With this input, the following physical model is proposed to explain the isolator shock foot unsteadiness. The approach boundary layer to the isolator upstream shock leg as well as the boundary layer immediately downstream of the shock leg provide broadband pressure fluctuations into the shock leg. The shock leg responds to the broadband input by selectively amplifying the low frequencies and the very high frequencies corresponding to boundary layer characteristic frequencies. Whereas the PSD of oscillations above $0.63f_c$ essentially mimic the incoming boundary layer spectrum, illustrating a simple amplification of incoming turbulence; the selective amplification at low frequencies needs further explanation and a simple physical model is presented below.

Consider a control volume as shown in figure 16 that bounds the incident and reflected oblique shock waves of the isolator duct (radius r) over a height of a boundary layer thickness (δ) and cross-sectional area (A). The streamwise length scales of the control volume (L and l) are both chosen of the order of a boundary layer thickness to emulate the length scale over which boundary layer fluctuations can make active contributions to the shock motion. The situation of interest is the upstream motion of the shock foot after it is displaced downstream by a high-momentum patch of the incoming boundary layer. Let us consider two instances: at $t = t_0$ when the shock foot has a velocity $u_s(l)$ and at a short time

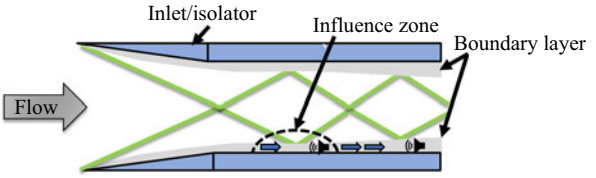

FIGURE 15. Illustration of the dominant sources that drive the shock oscillation at a given location.

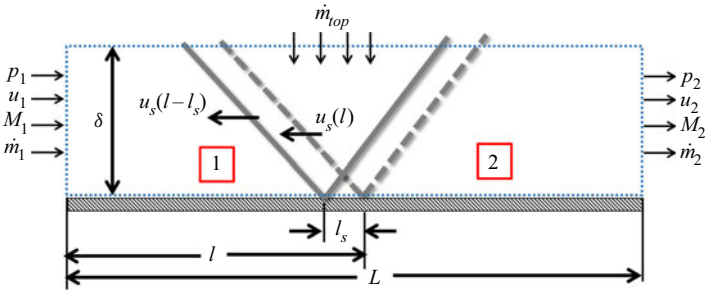

FIGURE 16. Control volume schematic of proposed shock unsteadiness model.

later $t = t_0 + \mathrm{d}t$ when the shock has moved a short distance l_s and has a velocity $u_s(l - l_s)$. The corresponding change in downstream pressure between the two time instances is Δp_3. For the sake of simplicity, the pressure and velocity fluctuations within the incoming boundary layer are neglected during this recovery time. Force balance equations in the frame of reference of the shock at these two time instances lead to the following:

$$\text{at } t = t_0: \quad \dot{m}(u_1 + u_s(l)) + \dot{m}_{top}u_{top} + p_1A = \dot{m}(u_{R3}) + p_3A + \tau_w(l)A_w(l), \tag{3.1}$$

$$\text{at } t = t_0 + \mathrm{d}t: \quad \dot{m}(u_1 + u_s(l - l_s)) + \dot{m}_{top}u_{top} + p_1A = \dot{m}(u_{R3} + \Delta u_{R3}) + (p_3 + \Delta p_3)A + \tau_w(l - l_s)A_w(l - l_s). \tag{3.2}$$

In the above equations, u_{R3} represents the velocity of the flow in region 3 in the shock frame of reference. For very small changes in the shock velocity, $\Delta u_s = u_s(l - l_s) - u_s(l)$, the corresponding change in the flow velocity relative to the shock is almost equal to Δu_s, i.e. $\Delta u_{R3} \approx \Delta u_s$ and the residual difference in momentum flux is much smaller than the unbalanced pressure force ($\Delta p_3 A$). Hence, for the purpose of this analysis, we assume $\Delta u_{R3} = \Delta u_s$ and $\dot{m}_{top}u_1$ remains unchanged.

Coming to the pressure excursion Δp_3, it can be shown that, for a shock angle of the incident shock of β, the corresponding pressure excursion across the incident shock Δp_2 for an inflow Mach number fluctuation ΔM_1 is given by

$$\Delta p_2 = p_1\left(\frac{2\gamma}{\gamma+1}2M_{1n} \times \Delta M_{1n}\right) = p_1M_1^2\sin^2\beta\left(\frac{2\gamma}{\gamma+1}\frac{2\Delta u_s}{u_1}\right), \tag{3.3}$$

$$\Delta p_2 A = \frac{2}{\gamma+1}\dot{m}\sin^2\beta \times 2\Delta u_s. \tag{3.4}$$

For flow turning angles that are modest, such as the case with unseparated shock boundary layer interactions, the pressure jumps between the two shocks are nearly

equally split; hence, the overall pressure excursion Δp_3 is twice Δp_2. That is,

$$\Delta p_3 A = 2\Delta p_2 A = 2 \times \frac{2}{\gamma+1}\dot{m}\sin^2\beta \times 2\Delta u_s. \tag{3.5}$$

As we approach the isolator SBLI region, the skin friction coefficient (C_f) would theoretically decrease from its incoming boundary layer value. The drop in C_f typically begins approximately one boundary thickness upstream and extends approximately one boundary layer thickness downstream of the shock impingement location. Subsequently, downstream, C_f recovers to a value that slightly exceeds the incoming boundary layer skin friction coefficient. Let C_{f1} represent an average skin friction coefficient in the upstream region until the shock impingement location and C_{f3} represent the average skin friction coefficient downstream of the shock impingement location. With these simplifications, the total friction force on the isolator wall within the control volume at the two time instances is given by

$$\tau_w(l)A_w(l) = \tfrac{1}{2}C_{f1}\gamma p_1 M_1^2 2\pi r l + \tfrac{1}{2}C_{f3}\gamma p_3 M_3^2 2\pi r(L-l), \tag{3.6}$$

$$\tau_w(l-l_s)A_w(l-l_s) = \tfrac{1}{2}C_{f1}\gamma p_1 M_1^2 \times 2\pi r(l-l_s) + \tfrac{1}{2}C_{f3}\gamma p_3 M_3^2 \times 2\pi r(L-l+l_s). \tag{3.7}$$

Further, for small values of Δu_s, it can be shown by using a Taylor series expansion that

$$\Delta u_s = \frac{\mathrm{d}u_s}{\mathrm{d}t}\frac{l_s}{u_s}. \tag{3.8}$$

In the above equation, the relation $u_s = \mathrm{d}l_s/\mathrm{d}t$ was employed during simplification. Subtracting (3.1) from 3.2, and using the expressions for the terms on the right-hand side, one obtains

$$0 = \frac{4}{\gamma+1}\dot{m}_1\sin^2\beta \times 2\frac{\mathrm{d}u_s}{\mathrm{d}t}\frac{l_s}{u_s} + \frac{1}{2}C_{f1}\gamma p_1 M_1^2\left(\frac{C_{f3}}{C_{f1}}\frac{p_3 M_3^2}{p_1 M_1^2} - 1\right)2\pi r l_s. \tag{3.9}$$

The above equation can be further simplified by noting $\dot{m}_1 u_1 = \gamma p_1 M_1^2 2\pi r\delta$ into

$$0 = \frac{8}{\gamma+1}\sin^2\beta\frac{\mathrm{d}u_s}{\mathrm{d}t} + \frac{C_{f1}u_1}{2\delta}\left(\frac{C_{f3}}{C_{f1}}\frac{p_3 M_3^2}{p_1 M_1^2} - 1\right)u_s, \tag{3.10}$$

which is of the form

$$\frac{\mathrm{d}u_s}{\mathrm{d}t} = -ku_s, \tag{3.11}$$

where

$$k = \frac{\gamma+1}{16\sin^2\beta}\frac{C_{f1}u_1}{\delta}\left(\frac{C_{f3}}{C_{f1}}\frac{p_3 M_3^2}{p_1 M_1^2} - 1\right). \tag{3.12}$$

This form of equation for the shock velocity is essentially identical to the model presented by Plotkin (1975) for shock oscillations over shock-induced separated flows. Whereas the factor k was experimentally determined in Plotkin's model (e.g. Poggie

& Smits 2005; Poggie *et al.* 2015), a theoretical determination is made here. The corresponding frequency multiplied pressure power spectrum is given by

$$fG(f) = 4p_{rms}f\frac{k}{k^2 + (2\pi f)^2}. \tag{3.13}$$

Figure 17 shows the predicted PSD using the current formulation beneath the isolator downstream shock leg and the corresponding experimental PSD. The value of p_{rms} was obtained from the experimental data integrating the PSD between $0.0063f_c$ and $0.063f_c$, and the choice of the frequency limits was made to adjust the predicted amplitudes to match with the experimental PSD. This method of computing p_{rms} may sound abnormal but is mathematically equivalent to using the typical definition on a signal that was band-pass filtered from $0.0063f_c$ and $0.063f_c$. The C_{f1} was set to 0.0014 (as measured from the boundary layer profile at $x/D = 6.30$) and the ratio C_{f3}/C_{f1} was varied between one and four. Evidently, the proposed physical model shows an excellent agreement with the measured spectrum over the entire band of low frequency oscillations up to $0.063f_c$ for $C_{f3}/C_{f1} \approx 1$–2 that are typically observed across SBLI, which provides significant credibility to the analysis and assumptions made. Interestingly, increasing C_{f3}/C_{f1} to four, which is quite high for attached SBLI situations, still keeps the shock oscillation spectrum in the ballpark of the observed low frequency range of shock oscillations, which serves to show that the analysis is fairly robust to the chosen value of the C_{f3}/C_{f1}. It should be noted that the unsteadiness of the pressure fluctuations of the upstream and downstream boundary layers that would serve as forcing functions of the shock oscillations has been ignored since their direct effects were observed only at high frequencies. Based on these observations, it appears that the low frequency shock oscillations are driven by the damping effect of the skin friction on the relaxing shock wave that is displaced by the boundary layer structures. Thus, the shock oscillations are driven rather indirectly by the boundary layers through the changes in skin friction coefficients across the SBLI, which explains the relatively modest coherence between the pressure fluctuations beneath the shock foot and boundary layers at these low frequencies.

3.6.1. *Comparison with other configurations*

Among the assumptions made in the previous analysis, the choice of the height of the control volume to be a boundary layer thickness needs to be re-examined as it ignores the possible impact of the duct diameter on the shock oscillations at very low frequencies. Furthermore, simplifying assumptions made on the shock jump relations as well as the shock velocities in relation to the relative velocities need to be further validated. Two further experimental configurations were tested to evaluate the above assumptions. The first configuration is an external flow SBLI where a 6° shock generator placed in a Mach 3 flow generated the shock interactions with the wind tunnel boundary layer that naturally transitioned to turbulence. This flow is an effectively unconfined flow and without the presence of multiple impinging/reflecting shocks; hence, this configuration corresponds to an 'infinite' duct diameter. The second configuration is that of the inlet/isolator used throughout this paper, but with a lesser inlet compression angle of 8°, which provides a smaller pressure rise across the shock waves. Both these measurements were made using the PCPSP technique, which provided spectra at frequencies up to $2.53f_c$.

Figure 18(*a*) shows the comparison of the experimentally obtained PSD beneath the shock foot of the external flow SBLI and the predicted PSD using the physical model. First and foremost, the unconfined SBLI with unseparated boundary layer also exhibits

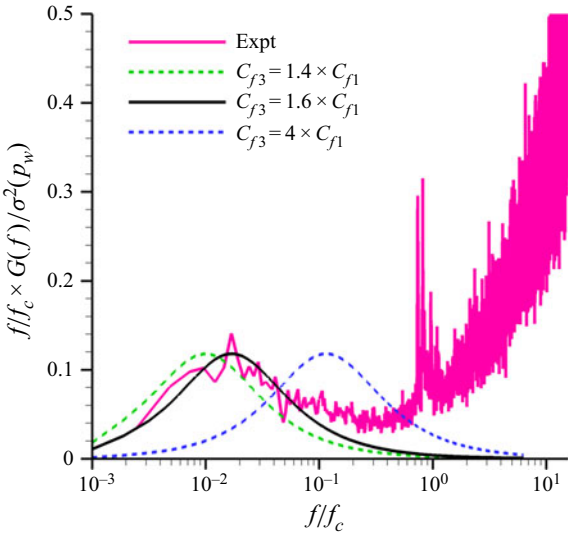

FIGURE 17. Comparison of PSD of the wall-pressure fluctuation from the proposed model and the experimental data for the isolator downstream shock leg.

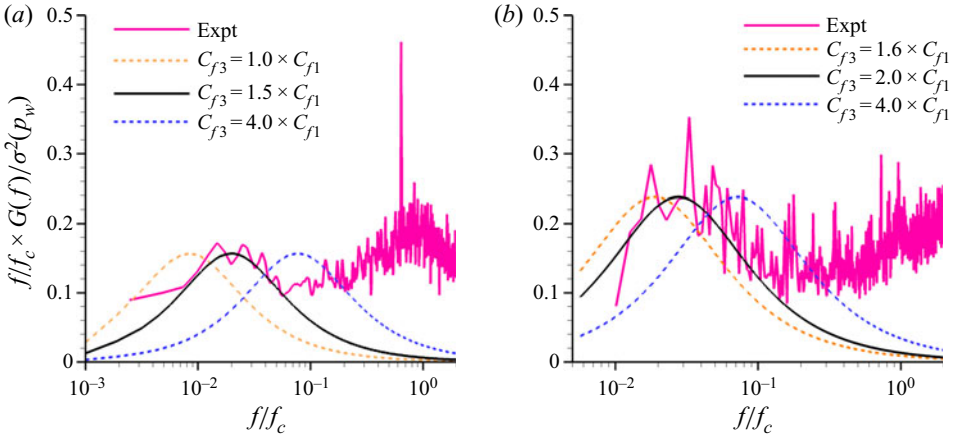

FIGURE 18. Comparison of wall-pressure fluctuation PSD from the proposed model and the measured PSD in: (*a*) an external unseparated shock boundary layer interaction unit; (*b*) inlet/isolator shock foot with 8° inlet compression angle.

the very low frequency oscillations at frequencies below $0.063f_c$, which are similar to inlet/isolator flows, as well as a sharp increase in PSD due to the amplification of the incoming turbulent boundary layer fluctuations. The predicted power spectra from the physical model also matched very well with the experimental dataset with the skin friction ratio C_{f3}/C_{f1} exhibiting very similar values as the inlet/isolator configuration. This excellent agreement provides compelling evidence that the shock oscillation phenomenon is indeed driven by the near-wall dynamics with very little contribution from the duct acoustics. A tight agreement was also obtained with the inlet/isolator flow fitted with an 8° inlet turn angle shown in figure 18(*b*), which further validates the simplifying assumptions made regarding the shock jumps and shock velocities.

4. Conclusions

An axisymmetric 2-D inlet/isolator was investigated to elucidate the shock foot dynamics and boundary layer fluctuation modifications that occur within the duct. The chosen inlet angles and application of no back pressure caused the boundary layer to remain attached across each shock impingement location along the entire duct length. The absence of local mean and instantaneous flow separations was also confirmed by multiple redundant measurements. Wall-pressure fluctuations were measured across two SBLI units that occurred within the inlet/isolator to shed light on the dynamics of pressure fluctuations and the shock foot oscillation spectrum. The shock foot pressure fluctuations on the other hand exhibit the high frequency content that arises from the passage of the boundary layer structures as well as a characteristic broadband hump at a very low frequency of the order of $0.03f_c$. This hump was not observed in either of the incoming or relaxing boundary layers. Further investigations revealed that these shock oscillations are caused by near-wall interactions that occurred within the local influence zone. A physical model is proposed that postulated the low frequencies result from the damping nature of the skin friction on the shock motions as the shock foot responds to the sudden excursions in the incoming boundary layer momentum. The PSD obtained from this model compared very well with both internal and external flow SBLI that maintained unseparated boundary layers.

Declaration of interests

The authors report no conflict of interest.

REFERENCES

BENDAT, J. & PIERSOL, A. 1986 *Random Data*, 2nd edn. John Wiley & Sons.

BRUCE, P. J. K. & BABINSKY, H. 2008 Unsteady shock wave dynamics. *J. Fluid Mech.* **603**, 463–473.

CARROLL, B. F. & DUTTON, J. C. 1990 Characteristics of multiple shock wave/turbulent boundary-layer interactions in rectangular ducts. *J. Propul. Power* **6** (2), 186–193.

CROCCO, L. 1958 *High Speed Aerodynamics and Jet Propulstion*. B, vol. 3. Princeton.

CURRAN, E. T. & STULL, F. E. 1964 The utilization of supersonic combustion ramjet systems at low Mach numbers. *Tech Rep.* RTD-TDR-63-4097. Aero Propulsion Lab.

FIÉVET, R., KOO, H., RAMAN, V. & AUSLENDER, A. H. 2017 Numerical investigation of shock-train response to inflow boundary-layer variations. *AIAA J.* **55** (11), 2888–2901.

FUNDERBURK, M. L. & NARAYANASWAMY, V. 2019 Spectral signal quality of fast pressure sensitive paint measurements in turbulent shock-wave/boundary layer interactions. *Exp. Fluids* **60** (10), 154.

GEERTS, J. S. & YU, K. H. 2016 Shock train/boundary-layer interaction in rectangular isolators. *AIAA J.* **54** (11), 3450–3464.

HUNT, R. L. & GAMBA, M. 2018 Shock train unsteadiness characteristics, oblique-to-normal transition, and three-dimensional leading shock structure. *AIAA J.* **56** (4), 1569–1587.

HUNT, R. L. & GAMBA, M. 2019 On the origin and propagation of perturbations that cause shock train inherent unsteadiness. *J. Fluid Mech.* **861**, 815–859.

IKUI, T., MATSUO, K. & NAGAI, M. 1974*a* The mechanism of pseudo-shock waves. *Bull. JSME* **17** (108), 731–739.

IKUI, T., MATSUO, K., NAGAI, M. & HONJO, M. 1974*b* Oscillation phenomena of pseudo-shock waves. *Bull. JSME* **17** (112), 1278–1285.

KORKEGI, R. H. 1975 Comparison of shock-induced two- and three- dimensional incipient turbulent separation. *AIAA J.* **26** (4), 534–535.

MILLER, J. H. 2018 Pressure scalings and influence region research. *Tech Rep.* AFRL Tech Briefs.

PICKLES, J. D., METTU, B. R., SUBBAREDDY, P. K. & NARAYANASWAMY, V. 2018 Gas density field imaging in shock dominated flows using planar laser scattering. *Exp. Fluids* **59** (112), 1–15.

PLOTKIN, K. J. 1975 Shock wave oscillation driven by turbulent boundary-layer fluctuations. *AIAA J.* **13** (8), 1036–1040.

POGGIE, J., BISEK, N. J., KIMMEL, R. L. & STANFIELD, S. A. 2015 Spectral characteristics of separation shock unsteadiness. *AIAA J.* **53** (1), 200–214.

POGGIE, J. & SMITS, A. J. 2005 Experimental evidence for Plotkin model of shock unsteadiness in separated flow. *Phys. Fluids* **17** (1), 018107.

RAMESH, M. D. & TANNEHILL, J. C. 2004 Correlations to predict the streamwise influence regions in supersonic turbulent flows. *J. Aircraft* **41** (2), 274–283.

SMITS, A. J. & MUCK, K.-C. 1987 Experimental study of three shock wave/turbulent boundary layer interactions. *J. Fluid Mech.* **182**, 291–314.

SU, W.-Y., JI, Y.-X. & CHEN, Y. 2016 Effects of dynamic backpressure on pseudoshock oscillations in scramjet inlet-isolator. *J. Propul. Power* **32** (2), 516–528.

SUGIYAMA, H., TAKEDA, H., ZHANG, J., OKUDA, K. & YAMAGISHI, H. 1988 Locations and oscillation phenomena of pseudo-shock waves in a straight rectangular duct. *JSME Intl J.* **31** (1), 9–15.

WALTRUP, P. J. & BILLIG, F. S. 1973 Structure of shock waves in cylindrical ducts. *AIAA J.* **11** (10), 1404–1408.

XIONG, B., FAN, X.-Q., WANG, Z.-G. & TAO, Y. 2018 Analysis and modelling of unsteady shock train motions. *J. Fluid Mech.* **846**, 240–262.

YAMANE, R., KONDO, E., TOMITA, Y. & SAKAE, N. 1984 Vibration of pseudo-shock in straight duct : 1st report, fluctuation of static pressure. *Bull. JSME* **27** (229), 1385–1392.